

Chapter 5

Casimir-Polder Force Measurement [3]

5.1 Introduction

The Casimir-Polder force is possibly the most fundamental interaction between an atom and a surface. This attractive atom-surface force is a consequence of the electromagnetic vacuum fluctuations that are predicted by QED. In particular, the surface imposes a spatial boundary condition on these vacuum fluctuations, and the resulting spatial dependence of these fluctuations induces an attractive force on the atom towards the surface.

For small atom-surface separations, often referred to as the van der Waals-London regime,¹ the attractive force is typically described in terms of the spontaneous electric dipole of an atom interacting with its image in the surface—similar to van der Waals force between two neutral atoms. The van der Waals-London potential near a perfectly conducting surface is

$$U_{vdw}(d) = -\frac{1}{4\pi\epsilon_0} \frac{\hbar}{4\pi d^3} \int_0^\infty \alpha(i\xi) d\xi, \quad (5.1)$$

where d is the atom-surface separation, and $\alpha(i\xi)$ is the polarizability of the atom evaluated along the imaginary axis. For our purposes, the integral in Eq. 5.1 can just be considered to encapsulate the dynamic polarizability of the atom.

¹ By small atom-surface distances we mean $d < \lambda/(2\pi)$, where λ is the wavelength of the dominant dipole transition of the atom. For rubidium $\lambda = 780$ nm, so this transition occurs at ~ 100 nm.

At larger atom-surface separations, retardation effects (due to the finite speed of light) of the virtual photons passing between the atom and its image causes the scaling behavior of the attractive force to change from $1/d^3$ to $1/d^4$. So, at large atom-surface separations, the potential is

$$U_{CP}(d) = -\frac{1}{4\pi\epsilon_0} \frac{3\alpha_0\hbar c}{8\pi d^4}, \quad (5.2)$$

where α_0 is the DC polarizability of the atom; this is the original Casimir-Polder result [6].

Potentials 5.1 and 5.2 are obtained by only considering the effects of the zero-temperature vacuum fluctuations. However, for non-zero temperatures, the effects of a populated photon blackbody again modify the scaling behavior.² For very large separations and non-zero temperatures the potential is

$$U_T(d) = -\frac{1}{4\pi\epsilon_0} \frac{\alpha_0 k_B T}{4d^3}, \quad (5.3)$$

where k_B is the Boltzmann constant and T is the temperature of the blackbody, which is typically set by the temperature of the surrounding objects.

In the interest of gaining some physical intuition into this force, it is worth going into some detail on the origin of Eq. 5.2 and 5.3. First, by examining Eq. 5.2 and 5.3, we see that in both cases the force is dependent on α_0 , the DC polarizability of the atom. This brings to mind the DC Stark shift that was introduced in the previous chapter:

$$U_E = -\frac{1}{4\pi\epsilon_0} \frac{\alpha_0}{2} E^2. \quad (5.4)$$

So, can we consider the Casimir-Polder force to be the attraction of the atom towards a “DC” electric field, or more precisely a region where the low-frequency electric field

² The crossover into this distance regime occurs at $d \sim (\hbar c)/(k_B T)$. At room temperature this occurs at $\sim 8 \mu\text{m}$.

fluctuations $\langle E^2 \rangle$ become large?³ In short, yes. Our goal is essentially then to determine $\langle E^2(d) \rangle - \langle E^2(\infty) \rangle$ as a function of distance to the surface d .⁴

Derivation of $\langle E^2(d) \rangle - \langle E^2(\infty) \rangle$ near a surface is a fine QED problem, but it is beyond the scope of this thesis. Thankfully this problem has been solved numerous times in physics literature, and the details are not particularly enlightening regarding the nature of the Casimir-Polder force. So, for this discussion, we will start with Eq. 3.94 of Section 3.12 from *The Quantum Vacuum* by Peter Milonni [51]. For the force on an atom near a conducting surface Milonni obtains:⁵

$$U(d) = \frac{1}{4\pi\epsilon_0} \frac{2\alpha_0\hbar c}{\pi} \int_0^\infty dk n_k k^3 \left(\frac{\sin(2kd)}{2kd} + \frac{2\cos(2kd)}{4k^2d^2} - \frac{2\sin(2kd)}{8k^3d^3} \right). \quad (5.5)$$

The variable k in Eq. 5.5 can be identified as $k = 2\pi/\lambda$, and n_k is the photon occupation of the k mode, so this integral is essentially summing over the contributions of different wavelengths in order to obtain the total $\langle E^2(d) \rangle - \langle E^2(\infty) \rangle$.

For the Casimir-Polder case, $n_k = 1/2$, so Eq. 5.5 becomes:

$$U(d) = \frac{1}{4\pi\epsilon_0} \frac{\alpha_0\hbar c}{\pi} \int_0^\infty dk k^3 \left(\frac{\sin(2kd)}{2kd} + \frac{2\cos(2kd)}{4k^2d^2} - \frac{2\sin(2kd)}{8k^3d^3} \right). \quad (5.6)$$

To evaluate the integral, we first make the substitution $u = 2kd$:

$$U(d) = \frac{1}{4\pi\epsilon_0} \frac{\alpha_0\hbar c}{\pi} \frac{1}{16d^4} \int_0^\infty du u^3 \left(\frac{\sin(u)}{u} + \frac{2\cos(u)}{u^2} - \frac{2\sin(u)}{u^3} \right). \quad (5.7)$$

Somewhat surprisingly, we see that the proper scaling behavior $1/d^4$ then appears. Evaluation of this integral will now only generate a numerical constant. To evaluate this highly oscillatory integral, we introduce a cutoff function $e^{-u\zeta}$, where ζ is a unit-less constant, that is removed after the integral is performed:

³ By low-frequency we mean frequencies lower than that corresponding to the dominant dipole transition.

⁴ We subtract $\langle E^2(\infty) \rangle$ to remove the infinite value of $\langle E^2 \rangle$ in free space.

⁵ The result Milonni obtains is for the $T = 0$ case, and so contains $1/2$ in the place of n_k .

$$U(d) = \frac{1}{4\pi\epsilon_0} \frac{\alpha_0 \hbar c}{\pi} \frac{1}{16d^4} \lim_{\zeta \rightarrow 0} \int_0^\infty du u^3 e^{-u\zeta} \left(\frac{\sin(u)}{u} + \frac{2\cos(u)}{u^2} - \frac{2\sin(u)}{u^3} \right). \quad (5.8)$$

We now have an integral that Mathematica can evaluate:

$$\lim_{\zeta \rightarrow 0} \int_0^\infty du u^3 e^{-u\zeta} \left(\frac{\sin(u)}{u} + \frac{2\cos(u)}{u^2} - \frac{2\sin(u)}{u^3} \right) = -6. \quad (5.9)$$

Finally, we can write the potential as

$$U(d) = \frac{1}{4\pi\epsilon_0} \frac{\alpha_0 \hbar c}{\pi} \frac{1}{16d^4} (-6) \quad (5.10)$$

$$= -\frac{1}{4\pi\epsilon_0} \frac{3\alpha_0 \hbar c}{8\pi d^4}. \quad (5.11)$$

This is exactly the Casimir-Polder result of Eq. 5.2.

We would now like to see the effect of changing the mode occupation number n_k in Eq. 5.5. The general form of the mode occupation number is

$$n_k = \frac{1}{e^{\frac{\hbar ck}{k_B T}} - 1} + \frac{1}{2}. \quad (5.12)$$

For the high temperature case, this can be reduced to

$$n_k \simeq \frac{k_B T}{\hbar ck}. \quad (5.13)$$

If we now use this in Eq. 5.5, instead of 1/2, the equation becomes:

$$U(d) = \frac{1}{4\pi\epsilon_0} \frac{2\alpha_0 T}{\pi} \int_0^\infty dk k^2 \left(\frac{\sin(2kd)}{2kd} + \frac{2\cos(2kd)}{4k^2 d^2} - \frac{2\sin(2kd)}{8k^3 d^3} \right). \quad (5.14)$$

We perform the same substitution as before and obtain

$$U(d) = \frac{1}{4\pi\epsilon_0} \frac{\alpha_0 k_B T}{4\pi d^3} \lim_{\zeta \rightarrow 0} \int_0^\infty du u^2 e^{-u\zeta} \left(\frac{\sin(u)}{u} + \frac{2\cos(u)}{u^2} - \frac{2\sin(u)}{u^3} \right). \quad (5.15)$$

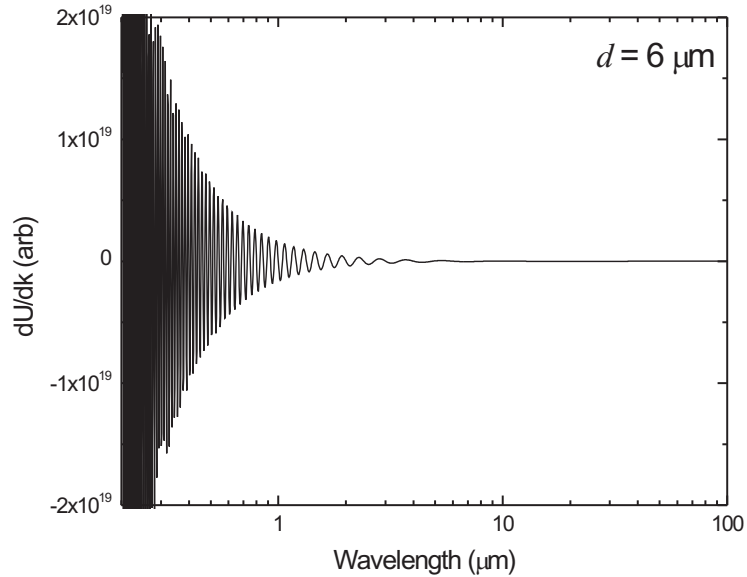


Figure 5.1: The integrand of Eq. 5.6 plotted as a function of wavelength ($2\pi/k$) for $d = 6 \mu\text{m}$. The divergent, oscillatory behavior at short wavelengths is apparent.

This integral can again be evaluated with Mathematica:

$$\lim_{\zeta \rightarrow 0} \int_0^{\infty} du u^2 e^{-u\zeta} \left(\frac{\sin(u)}{u} + \frac{2\cos(u)}{u^2} - \frac{2\sin(u)}{u^3} \right) = -\pi. \quad (5.16)$$

Finally, we obtain the potential in the high-temperature limit:

$$U(d) = -\frac{1}{4\pi\epsilon_0} \frac{\alpha_0 k_B T}{4d^3}. \quad (5.17)$$

Again, we obtain the correct result.

In addition to identifying the source of the crossover into the thermal regime, this derivation helps illuminate the source of the Casimir-Polder force. As was previously noted, the integral in Eq. 5.5 is summing the contributions from different wavelengths, so if we dwell for some time on this integrand we might hope to gain some physical insight into the nature of the Casimir-Polder force.

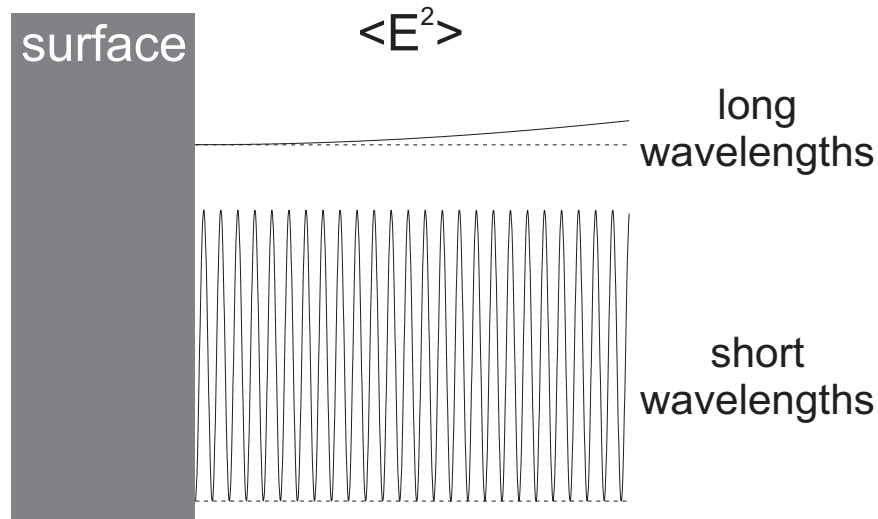


Figure 5.2: A simple diagram showing $\langle E^2 \rangle$ (solid lines, $\langle E^2 \rangle = 0$ is represented by the dashed lines) near the surface for long-wavelength (larger than the atom-surface separation) and short-wavelength (smaller than the atom-surface separation) photon modes. The minimum of $\langle E^2 \rangle$ at the surface causes $\langle E^2 \rangle$ to be small near the surface for the long wavelengths.

In Fig. 5.1, the integrand of Eq. 5.6 is plotted as a function of wavelength. The integrand is zero for long-wavelengths, and highly oscillatory and divergent for short-wavelengths. An interpretation of this behavior is as follows: The reflection off the surface of vacuum fluctuations at a given wavelength generates a standing-wave potential. As can be seen in Fig. 5.2, for long-wavelengths (larger than the atom-surface separation) $\langle E^2 \rangle$ is small due to the minimum at the surface. For short-wavelengths (smaller than the atom-surface separation), on the other hand, $\langle E^2 \rangle$ can be large and show significant spatial variation.⁶ There is an additional increase in the magnitude of $\langle E^2 \rangle$ for shorter wavelengths because the photon energy, and thus $\langle E^2 \rangle$, increases for

⁶ Oscillatory spatial behavior corresponds to oscillatory behavior in wavelength because changing the wavelength will change the standing-wave spacing. So, for short wavelengths $\langle E^2 \rangle$ at a given position will oscillate as the wavelength is changed.

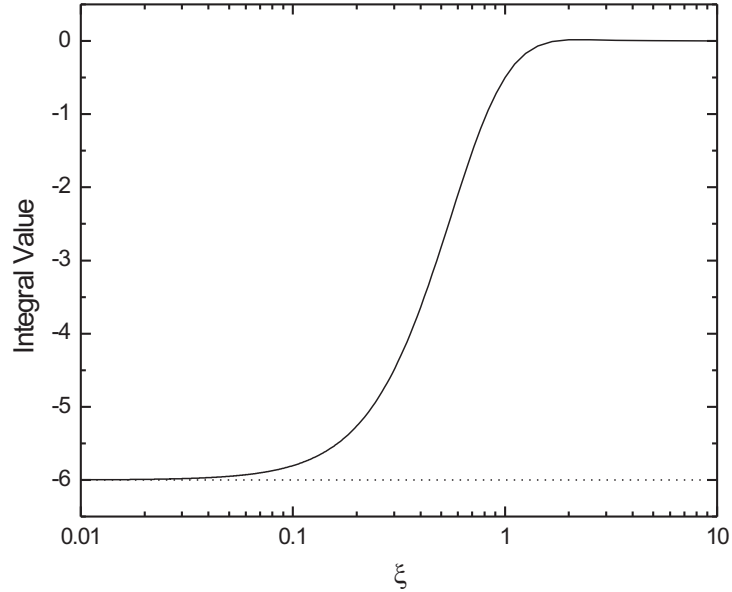


Figure 5.3: Plot of the value of the integral in Eqs. 5.9 as a function of the cutoff ζ . For $\zeta \simeq 0.18$ the integral is within $\sim 10\%$ of -6 , its asymptotic value.

short-wavelengths.

We can gain further insight into which wavelengths contribute to the Casimir-Polder force by inspecting the behavior of the cutoff function introduced in Eq. 5.8. In Fig. 5.3 we plot the value of the integral in Eq. 5.9. We see that for $\zeta \simeq 0.18$ the integral is within $\sim 10\%$ of its asymptotic value. In Fig. 5.4 we plot the integrand of Eq. 5.6 again; however, we now multiply by the cutoff function $e^{-2kd\zeta}$ (with $\zeta = 0.18$). The cutoff function suppresses the short-wavelength oscillations—apparently, the short-wavelengths average to zero in the integral, and thus do not contribute. The remaining contributions to the integral originate from wavelengths on the order of the atom-surface separation.

The integrand, however, still displays oscillatory behavior. This indicates that the Casimir-Polder force is resultant from the non-perfect cancellation of the contribution

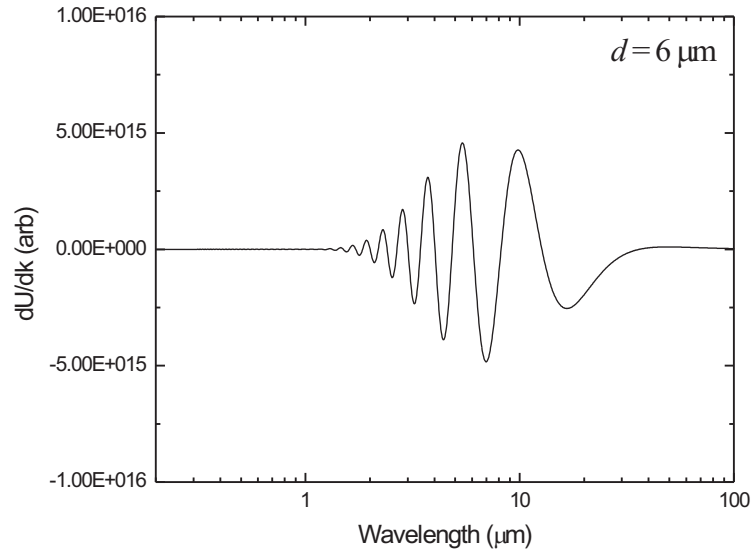


Figure 5.4: The integrand of Eq. 5.6 plotted as a function of wavelength ($2\pi/k$) for $d = 6 \mu\text{m}$ with the cutoff function $e^{-2kd\zeta}$ inserted. We set $\zeta = 0.18$, a value sufficient to provide a result within 10% of the asymptotic value. In contrast to Fig. 5.1, the short-wavelength oscillatory behavior is suppressed by the cutoff function, and it becomes clear the dominant wavelengths are those on the order of the atom-surface separation.

from these wavelengths. Additionally, the contribution of 10–100 μm wavelengths in Fig. 5.4 implies that increased occupation of these wavelengths, as is the case for room-temperature blackbody radiation, will have a significant influence on the Casimir-Polder force.

To this point, our discussion has only dealt with the Casimir-Polder force for a perfect conductor. The Casimir-Polder force can be similarly expressed for dielectric materials—in essence the theory must be modified for non-unity reflection, as well as transmitted and evanescent waves originating from the surface. Deriving the force in this situation was the focus of the recent paper by Antezza *et al.* [45], and the results of this paper are critical to interpreting the results of our experiment.

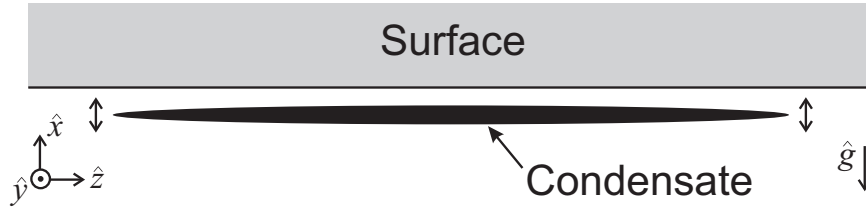


Figure 5.5: The coordinate definitions that will be used for the rest of this chapter.

5.2 Experimental Background

The experiment of Sukenik *et al.* [10] was the first to clearly measure the crossover from the van der Waals-London to the Casimir-Polder regime. This experiment measured the Casimir-Polder force by through a careful measurement of the opacity of a very narrow gold cavity with a beam of sodium atoms. They were able to quantitatively show an anomalous decrease in opacity, consistent with the Casimir-Polder force, from the cavity walls for cavity widths of 0.2–1 μm . A number of experiments have followed that use ultra-cold atoms to detect the presence of the Casimir-Polder force [11, 12, 52, 13, 38]; however, as of yet none have approached the sensitivity at large distances required to detect a crossover into the thermal regime.

Perhaps the most obvious technique for measurements of surface forces using ultra-cold atoms is interferometry in which atoms take separate spatial paths. This sort of atom-interferometry has proved difficult, but some groups have now started to make headway in this direction [53, 54, 55].

In our experiment, the effects of the surface potential on the *mechanical* motions of a Bose-Einstein condensate are studied. In particular, as was discussed in some depth in the previous chapter, we measure surface forces by detecting changes of the dipole oscillation frequency perpendicular to the surface. The normalized trap frequency change in the \hat{x} -direction [see Fig. 5.5] is defined as:

$$\gamma_x \equiv \frac{\omega_x - \omega'_x}{\omega_x}. \quad (5.18)$$

A simple approximation in terms of the second derivative was given in Eq. 4.2. For a measurement of the Casimir-Polder force, however, we must obtain γ_x in a more precise manner. In Antezza *et al.* [45], in addition to deriving the thermal Casimir-Polder force near a dielectric surface, the exact expression for γ_x from an arbitrary surface potential is derived. They found that the normalized frequency shift for a condensate from a surface potential $U(x)$, including the effects of finite oscillation amplitude a and a condensate Thomas-Fermi radius in the \hat{x} -direction of R_x , is

$$\gamma_x(d) = \frac{1}{2\pi m \omega_x^2} \frac{1}{a} \int_0^{2\pi} \int n_0^x(x) \frac{\partial U(d + a \cos(\phi))}{\partial x} dx d\phi, \quad (5.19)$$

where $n_0^x(x)$, the integrated one-dimensional condensate density profile, is defined as:

$$n_0^x(x) = \frac{15}{16} \frac{1}{R_x} \left(1 - \frac{x^2}{R_x^2}\right)^2. \quad (5.20)$$

To calculate the exact normalized frequency shift for a given surface potential we numerically integrate Eq. 5.19. The predicted γ_x using the results of [45] for a fused silica substrate and typical experimental parameters is plotted in Fig. 5.6. So, for plausible experimental conditions, the expected values of γ_x are on the order of 10^{-5} – 10^{-4} . Thus we must measure our radial trap frequency, typically 228 Hz in our experiments, to a precision of ~ 10 mHz. Obtaining this precision, although not straightforward, is certainly possible.

5.3 Experimental Procedure

Much of Chapter 2 was devoted to describing the experimental components and techniques that were developed in order to perform the Casimir-Polder measurement.

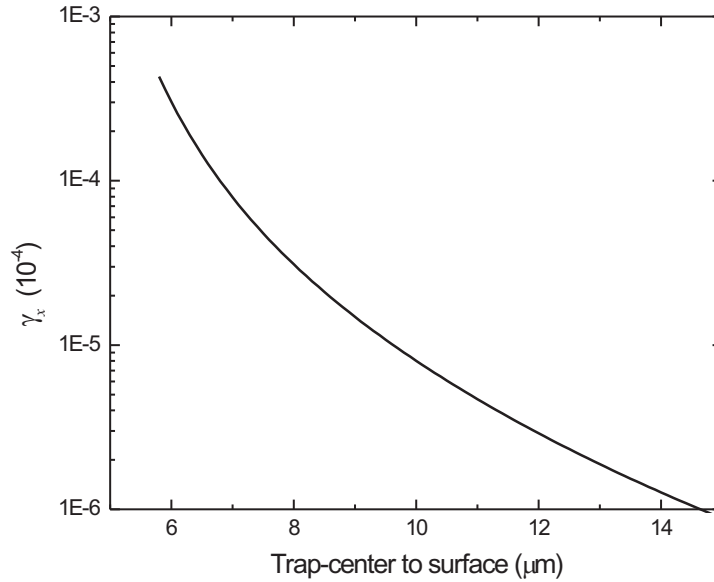


Figure 5.6: The predicted normalized frequency shift near a fused silica surface using the static approximation of [45]. The parameters corresponding to this plot, an oscillation amplitude of $2.1 \mu\text{m}$, a Thomas-Fermi radius of $2.4 \mu\text{m}$, and a radial frequency of 228 Hz, are typical values for our experiment.

The substrate setup for this experiment consisted of the pyrex surface holder and dielectric surfaces described in Section 2.2.2. We choose to replace the first set of surfaces in the titanium surface holder (described in Section 2.2.1 and used for the experiments of chapters 3 and 4) with a set of dielectric surfaces after discovering the alkali adsorbate problem that was discussed in the previous chapter. Additionally, the magnetic trap described in Section 2.2.5, the push coils and current servo described in Section 2.2.7, the radial oscillation excitation described in Section 2.3.3, the two-direction imaging described in Section 2.4.3, and the magnification measurement described in Section 2.4.4 were all developed for this Casimir-Polder experiment.

The measurement procedure for this experiment was quite similar to the experiment described in the previous chapter; however, it was necessary to take some addi-

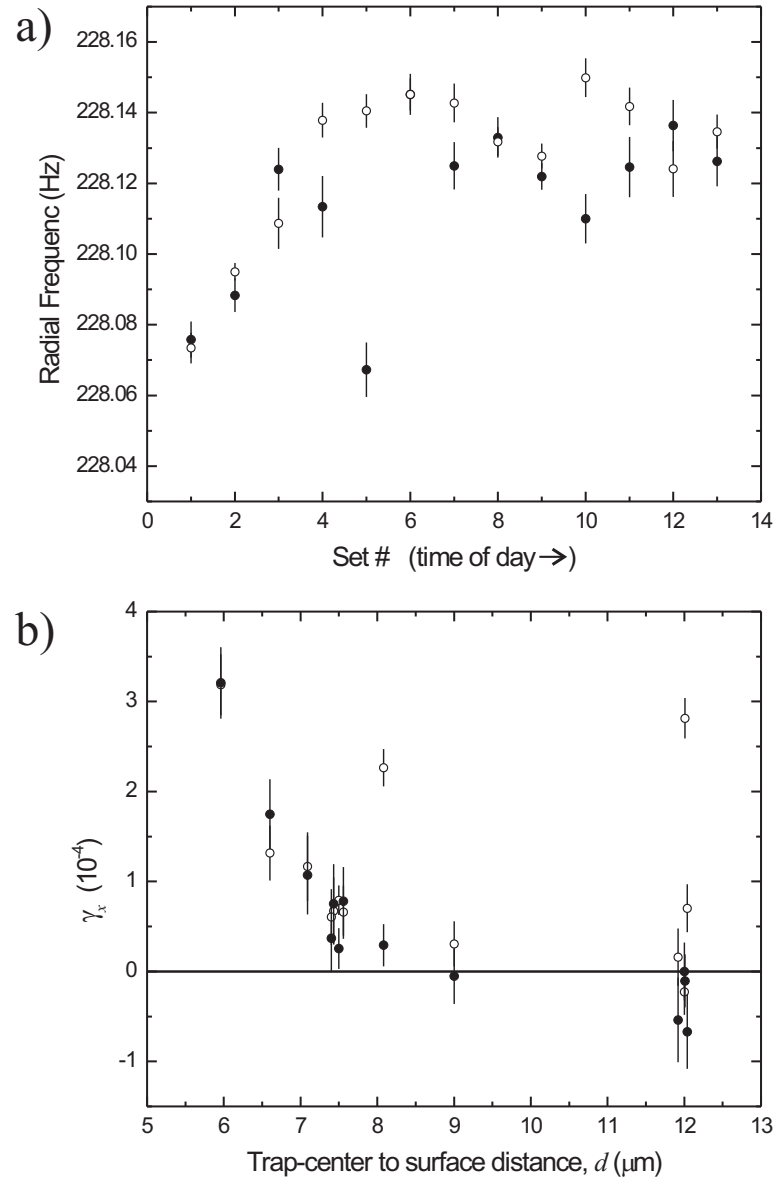


Figure 5.7: Raw experimental data highlighting the importance of taking concurrent normalization data. (a) Radial frequency data taken at a trap-center to surface distance d between 6 and 12 μm (solid points), and the 15 μm normalization distance (open points). (b) The normalized frequency shift γ_x as a function of d for the data from figure (a). The normalized frequency shift data calculated by using a fixed value (estimated to be 228.14 Hz) (open points) shows significantly more scatter than data normalized to the concurrently taken 15 μm point (solid points). The effect of the Casimir-Polder force for $d < 8 \mu\text{m}$ can be seen in both cases.

tional care in the determination of γ_x . We cannot simply take a number of data sets to measure the radial frequency ω_x as a function of distance to the surface, as is shown in Fig. 4.4, because the drift of the radial frequency over the day, caused by changes the temperature of the permanent magnets for instance, would introduce additional noise into the measurement.

Instead, data sets are taken that interleave vertical oscillation data at a desired trap-center to surface distance d , typically 6–12 μm , with vertical oscillation data taken at d_0 , the distance we use to obtain the normalization frequency ω_x . For this experiment we used $d_0 = 15 \mu\text{m}$. A distance of 15 μm is far away enough such that surface forces will not affect the frequency; the normalized dipole frequency shift from the Casimir-Polder force is less than 10^{-6} at this distance. By comparing the frequency measured at d to that measured at d_0 , we obtain γ_x at the particular condensate-surface separation d , and the measurement remains relatively immune to long-term drift of the radial trap-frequency. Finally, each radial frequency determination was “book-ended” between surface calibration data sets in order to get the most accurate determination of the trap-center to surface separation for a given measurement of γ_x .

5.3.1 Oscillation Frequency Measurement

At the end of Section 5.2 it was noted that in order to detect the Casimir-Polder force, the dipole frequency in the \hat{x} -direction must be measured to a precision of 10 mHz. In our experiment we have indeed achieved this, so it is worth a brief discussion of how this is accomplished. First, this precision is in large part possible because the radial dipole oscillation is very long lived. In fact, we have measured damping times of over 10 seconds. Thus, by measuring the oscillation over several seconds the phase sensitivity (or signal-to-noise) necessary to measure a frequency to 10 mHz is reasonable. This can be seen with the following equation:

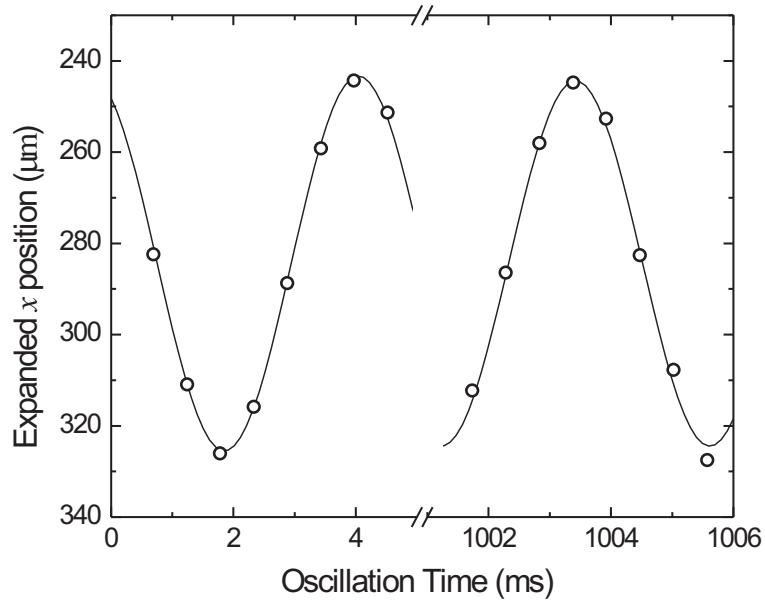


Figure 5.8: Typical data from the radial dipole oscillation. This plot (also shown in the previous chapter) clearly illustrates the long damping time of the radial dipole oscillation mode.

$$\delta\nu = \frac{1}{2\pi T(s/n)\sqrt{N}}, \quad (5.21)$$

where $\delta\nu$ is the frequency uncertainty, T is the measurement, or “interrogation” time, N is the number of measurements, and s/n is the signal-to-noise ratio. So, $\delta\nu = 10$ mHz, $T = 1$ second, and $N = 10$ a signal-to-noise ratio of only 5 is necessary.⁷ This means that for our $2 \mu\text{m}$ oscillation amplitude (our signal), there can be no more than 400 nm of in-trap vertical position noise.

Reexamining Eq. 5.21, it seems clear that to obtain the most precise frequency measurement we should use the longest interrogation time possible. There are, however, several subtle tradeoffs involved. First, the oscillation amplitude is a parameter that

⁷ Ten points is a typical number of data points in a set. At one data point per minute, this data set would require 10 minutes.

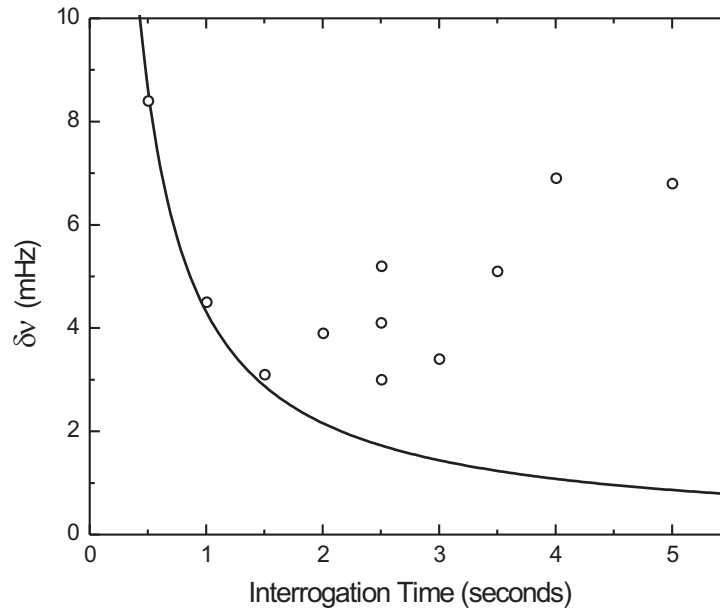


Figure 5.9: The frequency uncertainty as a function of interrogation time (open points). The first three points are fit to the form of Eq. 5.21 (solid line), for these points the signal-to-noise is ~ 12 . The frequency uncertainty for the later points clearly does not follow this trend, and instead is limited by ~ 5 mHz of phase noise. The 5 mHz of radial trap frequency phase noise is due to ~ 0.1 °C temperature drifts of the the permanent magnets.

enters into the calculation of the predicted frequency shift from the Casimir-Polder force [see Eq. 5.19], so it is undesirable for its value to change significantly over a frequency measurement—this already limits us to interrogations times significantly shorter than the damping time. Second, Eq. 5.21 assumes that the noise does not *increase* as a function of interrogation time; however, this is exactly what happens in the case of phase noise. In Fig. 5.9 the frequency uncertainty as a function of interrogation time is plotted. The frequency uncertainty for interrogation times up to ~ 1.5 seconds follow Eq. 5.21; however, the frequency uncertainty for longer interrogation times levels off at about 5 mHz, and then increases.

We have correlated this phase noise with temperature drifts of ~ 0.1 °C of the permanent magnets over the course of a data set. In the future, it might be worth attempting to further stabilize the temperature of these magnets; however for these experiments we simply restricted our data taking to interrogation times of 0.5–1.5 seconds.

Finally, the *manner* in which the oscillation data is taken is of some importance. In Fig. 5.8 the oscillation data only shows a single radial oscillation period at a short-time and a single oscillation period at a long-time; this is the optimum manner in which to take data. The short-time “fringe” fixes the initial oscillation phase. The long-time fringe measures the phase evolution that has occurred over the interrogation time. An additional fringe taken at an intermediate time would serve neither role very well. This is equivalent to fitting a line to a set of data points: the points at the extremes play the most important role in the linear fit. The only precaution to this method of data taking is that (1) you must be certain that the phase evolves in a linear manner (the frequency is not chirping) and (2) the frequency must be known to a sufficient precision to ensure that there is no aliasing.⁸ We spent a good deal of time verifying that the phase does evolve in a linear manner, and we additionally vary the interrogation between 0.5 and 1.5 seconds for each frequency measurement.

The problem of frequency chirps brings us to our the final point with regard to frequency measurement. We found, in a somewhat painful manner, that it is not advisable to trigger an experiment off of 60 Hz. By doing this, small, effectively randomly changing fields are transformed into small fields that are reproducible for every experiment realization, and thus do not average away. In fact, we discovered a very small frequency chirp in our vertical oscillation that was caused by a very small (< 100 nm) in-trap motion being driven by magnetic field noise at 240 Hz (4×60 Hz). By simply triggering the experiment instead off a random trigger, this small in-trap motion was

⁸ For instance, with an interrogation time of 1 second the frequency can be fit to a number of different values 1 Hz ($1/T$) apart. So it is necessary to know the frequency to better than 1 Hz in order to use an interrogation time of 1 second.

converted back into random noise, and our small frequency chirp averaged away.

5.4 Systematics

Rejection of the presence of spurious forces on the condensate caused by surface-based electric and magnetic fields is critical to the interpretation of our results. We spent a significant amount of time dedicated to understanding the systematics that we are sensitive to, and to developing a set of procedures to allow us to quantify them.

5.4.1 Spatially Inhomogeneous Forces

Our most powerful test for spurious forces is provided by the elongated geometry of our BEC. The mean atom-surface separation for our closest measurements, $\sim 6 \mu\text{m}$, is significantly smaller than the axial extent of the BEC, $\sim 170 \mu\text{m}$. Thus a spatially inhomogeneous force, due to localized electric or magnetic surface contamination, would likely only effect part of the BEC (The case of spatially uniform forces will be covered in Sections 5.4.3 and 5.4.4). When oscillating in this inhomogeneous potential, the BEC behaves much more like a string than a bar, and will oscillate at different radial frequencies along its axial extent. We then can perform analysis of γ_x along the axial extent of the BEC. We have been performing axial analysis of our BEC and normal clouds for some time⁹ —the elongated geometry of our trapped cloud clearly favors axial structure over radial structure, and thus is conducive to such analysis.

In order to obtain axial profiles of γ_x we perform the following: First, when taking a typical data set of vertical oscillation data, we save the side-view images, in addition to the parameters from the side-view and end-view fits for each data point [see Section 2.4.3]. Each side-view image is then analyzed, and vertical density cuts are fit to Gaussian profiles in order to obtain a value for the center of the BEC at a given axial point [see Fig. 5.10 (a) and (b)]. This is performed at many points along the axis of

⁹ For instance our spin wave [56] and spin locking work [57].

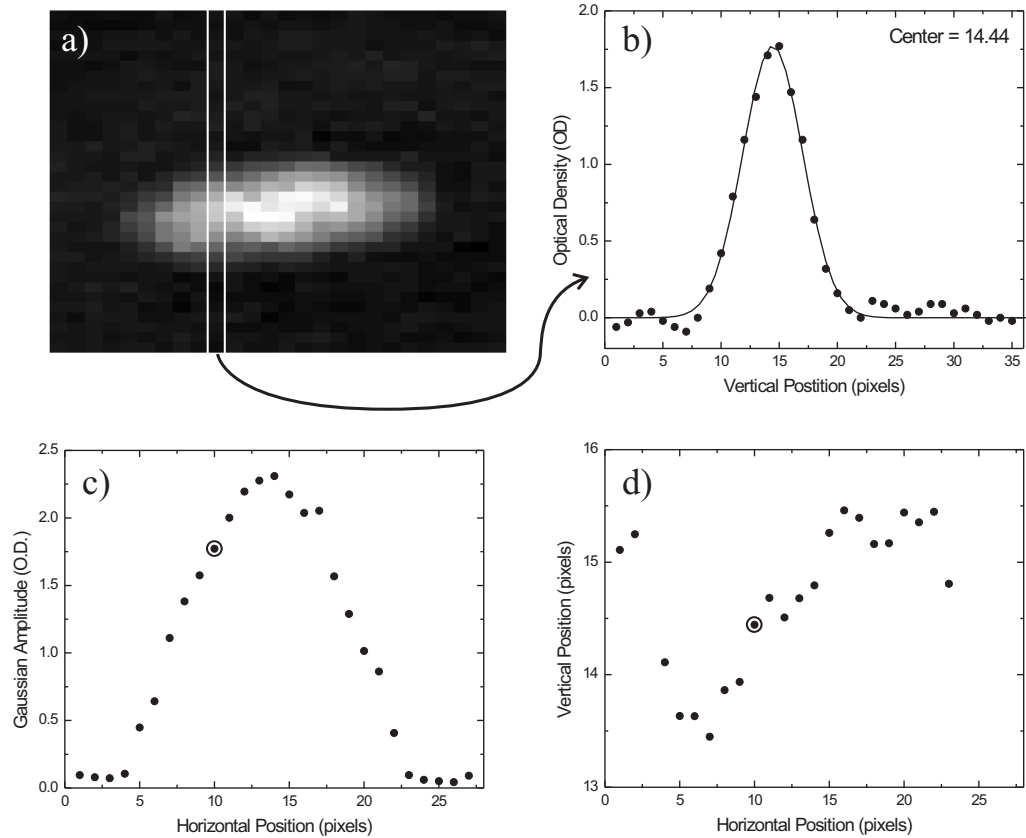


Figure 5.10: The procedure used to find the vertical center across the BEC. (a) An image of an expanded BEC after one second of oscillation 15 microns from our fused silica surface. (b) A vertical cut through the image. The row of pixels for the cut is highlighted by the white vertical lines in (a). The profile is fit to a Gaussian to obtain the vertical center of the density cut. (c) The Gaussian fit amplitude for each vertical cut across the image – the Thomas-Fermi profile can clearly be seen here. The circled point is from the vertical profile shown in (b). (d) The fit vertical center for each vertical cut along the image. Again, the circled point is from the vertical profile shown in (b).

the BEC, and we obtain the profile of the vertical center across the axis of the BEC [see Fig. 5.10 (c) and (d)]. After the vertical center profile is obtained for each image in the data set, we then fit the oscillation frequency for each axial point. This results in a profile of the vertical frequency across the BEC [see Fig. 5.11 (a)]. Finally, we calculate γ_x for each point along the axis of the BEC, as is shown in Fig. 5.11 (b).

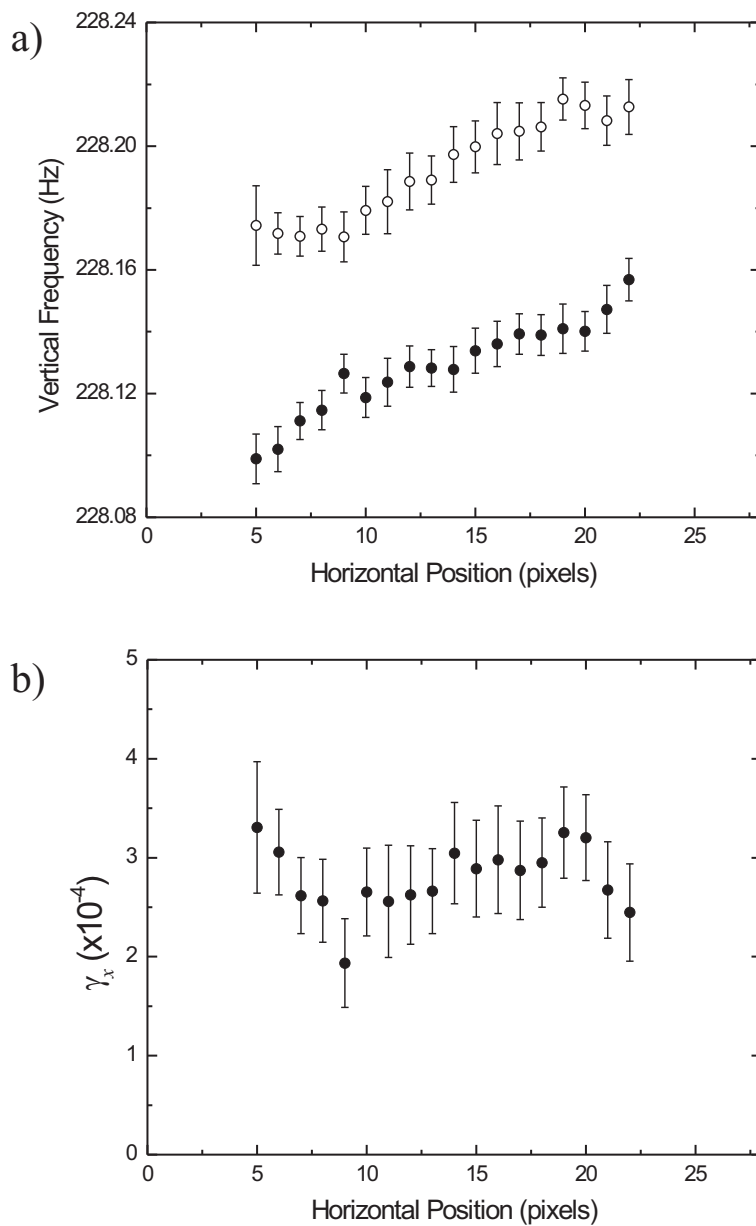


Figure 5.11: (a) The fit frequency across the BEC. The solid (open) points were taken 6 (15) μm from the surface. (b) The calculated normalized frequency shift $\gamma_x(z)$ across the BEC from the 6 and 15 μm data in (a).

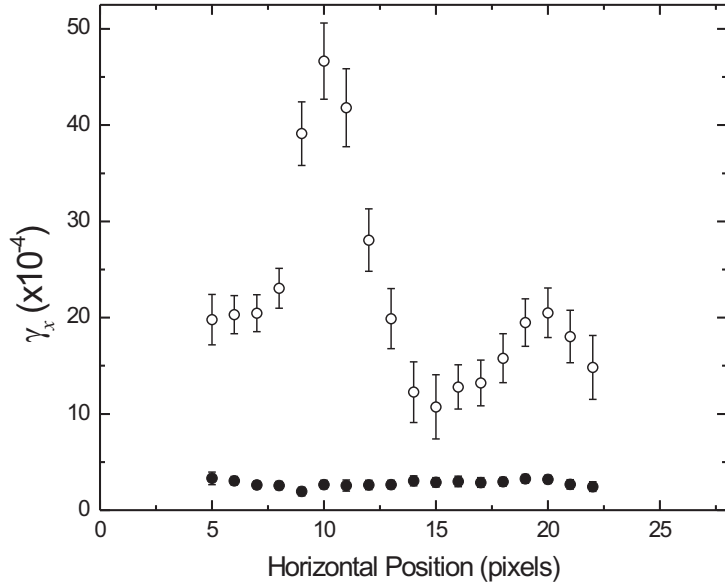


Figure 5.12: Open points show data taken over a surface (sapphire) displaying very large, spatially inhomogeneous forces. For comparison, the data from Fig. 5.11 (b) is plotted as well (solid points).

The linear frequency shift across the cloud in Fig. 5.11 (a) is due to a small excitation of the “scissors” mode [58]. For axial positions away from the \hat{z} -center of the trap, the changing gradient of the \hat{z} -component of the magnetic field, provided by the pinch coils, breaks the symmetry of the \hat{x} and \hat{y} linear magnetic fields gradients. This causes a linear change in ω_x and ω_y along the \hat{z} -axis. This linear change in ω_x appears in both the 6 and 15 μm data in Fig. 5.11 (a), thus it will not appear in $\gamma_x(z)$ along the BEC [see Fig. 5.11 (b)].

The data in Fig. 5.11 (b) showing $\gamma_x(z)$ along the BEC appears to be statically consistent with no significant spatially inhomogeneous forces. So what does a “bad” $\gamma_x(z)$ profile, indicating inhomogeneous forces, look like? Shown in Fig. 5.12 is data taken near our sapphire surface, which displayed very large spatially inhomogeneous

forces. For comparison, the data from Fig. 5.11 (b) is reproduced in this figure as well (solid points). The presence of spatially inhomogeneous forces is apparent simply through visual inspection in these two extreme examples, but we clearly need a more quantitative method for evaluating these $\gamma_x(z)$ profiles.

To quantify the presence of spatially inhomogeneous forces we take the root mean square (rms) deviation of $\gamma_x(z)$ along the BEC, and obtain δ_γ . We then compare δ_γ to the statistical error in γ_x determined from the center-of-mass fits, $\sigma\gamma_x$. If $\delta_\gamma > \sigma\gamma_x$, then we surmise that there is a statistically significant spatially inhomogeneous force acting on the condensate, and thus move to a new surface location. On the other hand, if $\delta_\gamma < \sigma\gamma_x$, then we take δ_γ to be our systematic limit on spatially inhomogeneous forces experienced by the condensate.¹⁰

5.4.2 Spatially Homogeneous Forces

Spatially uniform spurious shifts along the extent of the condensate are less likely, but must also be accounted for. A completely uniform surface charge, or magnetization, will by symmetry not generate a force. The remaining possible cause of spurious uniform forces is then stripes of surface contaminations collinear with the axis of the condensate. This is not such an unlikely situation. In our work studying alkali adsorbates, discussed in the previous chapter, we measured electric fields from alkali atoms adsorbed onto surfaces. The spatial distribution of atoms that adsorb onto the surface from the condensate will reflect the dimensions of the condensate and thus essentially form an elongated stripe of electrical dipoles collinear to the axis of the condensate. So, to test for this possibility, we perform measurements at multiple surface locations, as well as a series of measurements to test for the presence of magnetic and electric fields.

¹⁰ This definition, although somewhat arbitrary, carries significance because if δ_γ is much larger than $\sigma\gamma_x$, then there is certainly a significant spatially inhomogeneous force present as is clearly the case in Fig. 5.12.

5.4.3 Spatially Homogeneous Electric Forces

As has been noted many time thus far in this thesis, an atom in an electric field will experience an energy shift according to $U_E = -(\alpha_0/2)E^2$, where α_0 is the ground state DC polarizability and E is the electric field magnitude. Thus, to first approximation (using Eq. 4.2), the normalized frequency shift caused by an electric field can be written as

$$\gamma_x \propto -\partial_x^2 U_E = \frac{\alpha_0}{2} \partial_x^2 [(E_x^*)^2 + (E_y^*)^2 + (E_z^*)^2]. \quad (5.22)$$

Our goal is then to determine $E_x^*(x)$, $E_y^*(x)$, and $E_z^*(x)$; from these we can obtain an estimate of γ_x . In our studies of alkali adsorbates in Chapter 4 we apply a uniform external electric field E_x^{ext} . By measuring a change in γ_x as E_x^{ext} is varied ± 100 V/cm we obtain $\partial_x^2 E_x^*(x)$. For the work of this chapter, we instead use a technique that allows us instead to measure $\partial_x E_x^*(x)$, as well as $\partial_x E_y^*(x)$ and $\partial_x E_z^*(x)$.

If, rather than apply a DC external electric field, we apply an AC external electric field $E_x^{ext} \cos(\omega t)$, where $E^{ext} \gg E^*$, then the forces on the atoms are

$$F_x(t) \simeq \alpha_0 E_x^{ext} \cos(\omega t) \partial_x E_x^* \quad (5.23)$$

$$F_y(t) \simeq \alpha_0 E_x^{ext} \cos(\omega t) \partial_y E_x^*$$

$$F_z(t) \simeq \alpha_0 E_x^{ext} \cos(\omega t) \partial_z E_x^*.$$

We then invoke $\vec{\nabla} \times \vec{E} \simeq 0$,¹¹ allowing us to then rewrite the forces on the atoms as

$$F_x(t) \simeq \alpha_0 E_x^{ext} \cos(\omega t) \partial_x E_x^* \quad (5.24)$$

$$F_y(t) \simeq \alpha_0 E_x^{ext} \cos(\omega t) \partial_x E_y^*$$

$$F_z(t) \simeq \alpha_0 E_x^{ext} \cos(\omega t) \partial_x E_z^*.$$

¹¹ $\partial \vec{B} / \partial t$ due to the charging and discharging of the plates is extremely small and can be safely neglected.

If ω is set to ω_x , ω_y , or ω_z , and $\partial_x E_{x,y,x}^*$ is nonzero, the oscillating electric field will resonantly drive a dipole oscillation. This allows the measurement of what normally would be very small forces. By keeping the drive time short, 50–100 ms in our experiment, compared to oscillation damping rate, typically 1–10 s, and the inverse of the drive detuning, typically < 0.5 Hz, then the system reduces to that of a undamped, resonantly driven oscillator.

The equation of motion of an undamped resonantly driven oscillator, initially at rest, is

$$x(t) = \frac{F_0}{2\omega m} t \sin(\omega t) \quad (5.25)$$

where F_0 is the driving force, ω is the natural frequency of the oscillator and the frequency of the drive, and m is the mass of the oscillator. The oscillation amplitude thus linearly grows as

$$\dot{A} = \frac{F_0}{2m\omega}. \quad (5.26)$$

Looking at Eqs. 5.24, we can identify F_0 in the \hat{x} , \hat{y} , and \hat{z} -directions as

$$F_{0,i} = \alpha_0 E_x^{ext} \partial_x E_i^* \quad (5.27)$$

where we are using \hat{i} as shorthand for the \hat{x} , \hat{y} , or \hat{z} -direction. Using Eq. 5.25 and 5.27 we can express $\partial_x E_i^*$ in terms of the growth rate \dot{A} as

$$\partial_x E_i^* = \frac{2m\omega_i \dot{A}_i}{\alpha_0 E_x^{ext}}. \quad (5.28)$$

To measure $\partial_x E^*$, we do the following: We position a BEC a given distance from the surface and drive a large external electric field $E_x^{ext} \simeq 100$ V/cm at a given trap frequency ω_i , and then measure the amplitude growth rate in the \hat{i} -direction. So, to measure the amplitude growth rate \dot{A} in the \hat{x} and \hat{y} -directions, we drive the external

Table 5.1: A table showing how limits on γ_x from uniform electric fields are obtained from the fits from Fig. 5.14. For each value of p and C_y γ_x and $\sigma\gamma_x$ is calculated for $x = 5 \mu\text{m}$.

p	C_y V m^{p-1}	σC_y V m^{p-1}	γ_x $\times 10^{-5}$	$\sigma\gamma_x$ $\times 10^{-5}$	$\gamma_x + \sigma\gamma_x$ $\times 10^{-5}$
0.2	26.0	3.7	0.89	0.25	1.14
0.5	0.29	0.03	0.60	0.12	0.72
1.0	3.6×10^{-4}	0.3×10^{-4}	0.55	0.09	0.65
2.0	1.0×10^{-9}	0.1×10^{-9}	0.58	0.08	0.67

electric field at ~ 228 Hz and look for growing oscillations in the \hat{x} and \hat{y} directions. To measure \dot{A} in the \hat{z} -direction, we drive the external electric field at ~ 6.4 Hz, and look for growing oscillations in the \hat{z} -direction.

An amplitude growth rate can then be converted into $\partial_x E_i^*$ using Eq. 5.28. This is performed at multiple distances from the surface. Finally we obtain a series of points to allow us to estimate $\partial_x E_i^*(x)$. A typical set of $\partial_x E_i^*(x)$ points is shown in Fig. 5.13.

As previously mentioned, our ultimate goal is to obtain estimates for $E_i^*(x)$ that we can simply insert into Eq. 5.22 to obtain a limit for γ_x from uniform electric forces. To get $E_i^*(x)$ from the $\partial_x E_i^*(x)$ data in Fig. 5.13 we fit the data to the form

$$\partial_x E_i^*(x) = -p_i \frac{C_i}{x^{p_i+1}}. \quad (5.29)$$

$E_i^*(x)$ is then simply

$$E_i^*(x) = \frac{C_i}{x^{p_i}}. \quad (5.30)$$

Finally, combining Eq. 5.22 and 5.30, we can write γ_x for a given $E_x^*(x)$, $E_y^*(x)$, and $E_z^*(x)$ in terms of C_i and p_i as

$$\gamma_x(x) = \frac{\alpha_0}{2m\omega_x^2} \frac{C_i^2 p_i}{x^{2p_i+2}} (2p_i + 1). \quad (5.31)$$

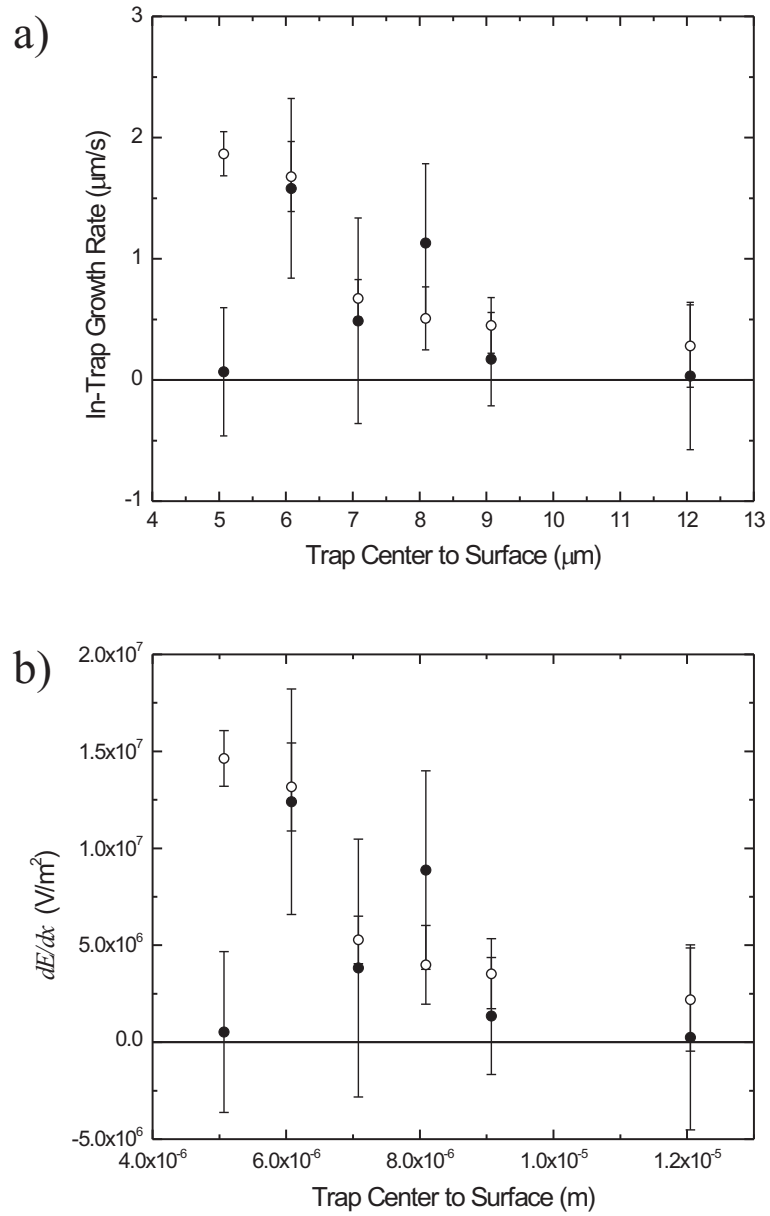


Figure 5.13: (a) The measured growth rate in the \hat{x} (solid points) and \hat{y} -directions (open points) at several distances. An ~ 100 V/cm ($\sim 10^4$ V/m) oscillating electric field amplitude was used for this data. (b) The growth rate from (a) converted into $\partial_x E_x^*(x)$ (solid points) and $\partial_x E_y^*(x)$ (open points).

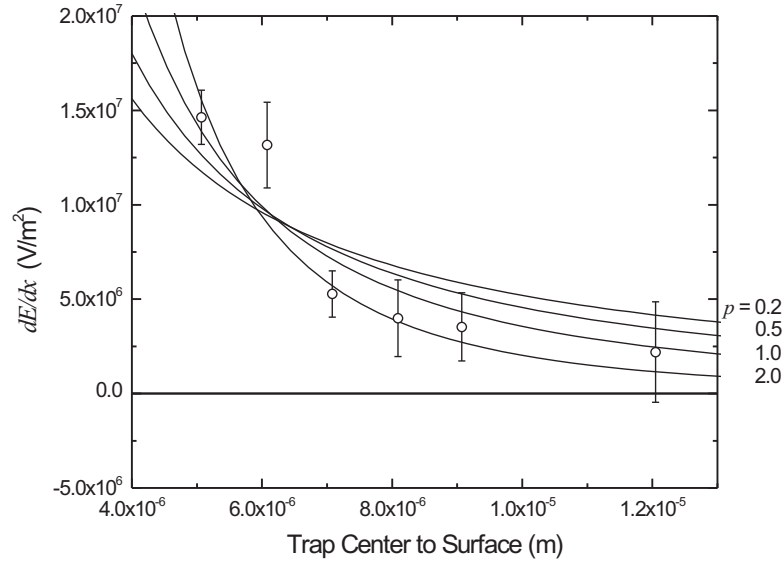


Figure 5.14: An example showing fitting of the $\partial_x E_y^*(x)$ data from Fig. 5.13 to the form of Eq. 5.29 with $p = 0.2, 0.5, 1.0, 2.0$.

Looking at the growth rate data in Fig. 5.13, it is clear that the data is not sufficiently clean as to allow a simultaneous fit of both the p_i and C_i parameters—doing this gives nonsensically large error bars for both parameters. What we do instead is to perform weighted fits¹² to the data by fixing p_i to a range of values from 0.2, corresponding to a very broad collinear surface potential, to 2.0, corresponding to a line of dipoles. For each value of p_i we obtain a fit value C_i and error σC_i . We then, in addition to obtaining a value for γ_x , can get $\sigma\gamma_x$ as

$$\sigma\gamma_x(x) = \frac{\alpha_0}{2m\omega_x^2} \frac{2(C_i \sigma C_i)p_i}{x^{2p_i+2}} (2p_i + 1). \quad (5.32)$$

We could then subtract γ_x from the data, and assign the electric systematic uncertainty as $\sigma\gamma_x$; however because we obtain C_i by fixing the power p_i , we can have little confidence that we are using the correct form for the electric field. So instead, we

¹² Weighting is assigned by the vertical error bars.

simply add γ_x and $\sigma\gamma_x$ to assign a total electric systematic limit.

Finally, in practice we have found that contributions from E_z^* can be neglected. Numerically, this can be seen from Eq. 5.28 and 5.31. For a fixed growth rate \dot{A} , the dependence on trap frequency ω_i is quadratic. Therefore, for the contribution from the \hat{z} -direction to equal those from the \hat{x} and \hat{y} -directions, the growth rate in the \hat{z} -direction must be ~ 1000 times larger than that measured in the \hat{x} and \hat{y} -directions, and we have never measured a \hat{z} -growth rate significantly larger than those measured the \hat{x} and \hat{y} -directions. The physical explanation for this is that the axial direction is averaging over $\sim 170 \mu\text{m}$, making it extremely improbable that E_z^* could contribute to a uniform spurious electric field force. This returns us to the argument in Section 5.4.2 where we concluded that uniform electric and magnetic forces on the condensate could only be caused by collinear distributions, thus it is not surprising that contributions from E_z^* are small.

The last consideration regarding our electric field calculation in the actual electric field applied to the position of the condensate by our electric field plates.¹³ Fig. 5.15 shows the results from calculations that we performed using Ansoft electrostatic field simulation software. The net effect of the dielectric materials is to slightly increase the electric field at the position of the condensate. From Fig. 5.16 we see that the electric field is rather uniform in the vertical direction; however there is clearly some uncertainty the precise value of the electric field, so for our calculations we choose a somewhat conservative value of 100 V/cm for the amplitude of the external applied electric field.

¹³ We are not applying a DC electric field, but an electric field oscillating at 228 Hz. This permits our force detection technique previously described and prevents the dielectric materials from charging up. This drive frequency, 228 Hz, is extremely low compared to resonances in the dielectric response of the atoms and the solids, and so can be considered to be DC for the purposes of these simulations.

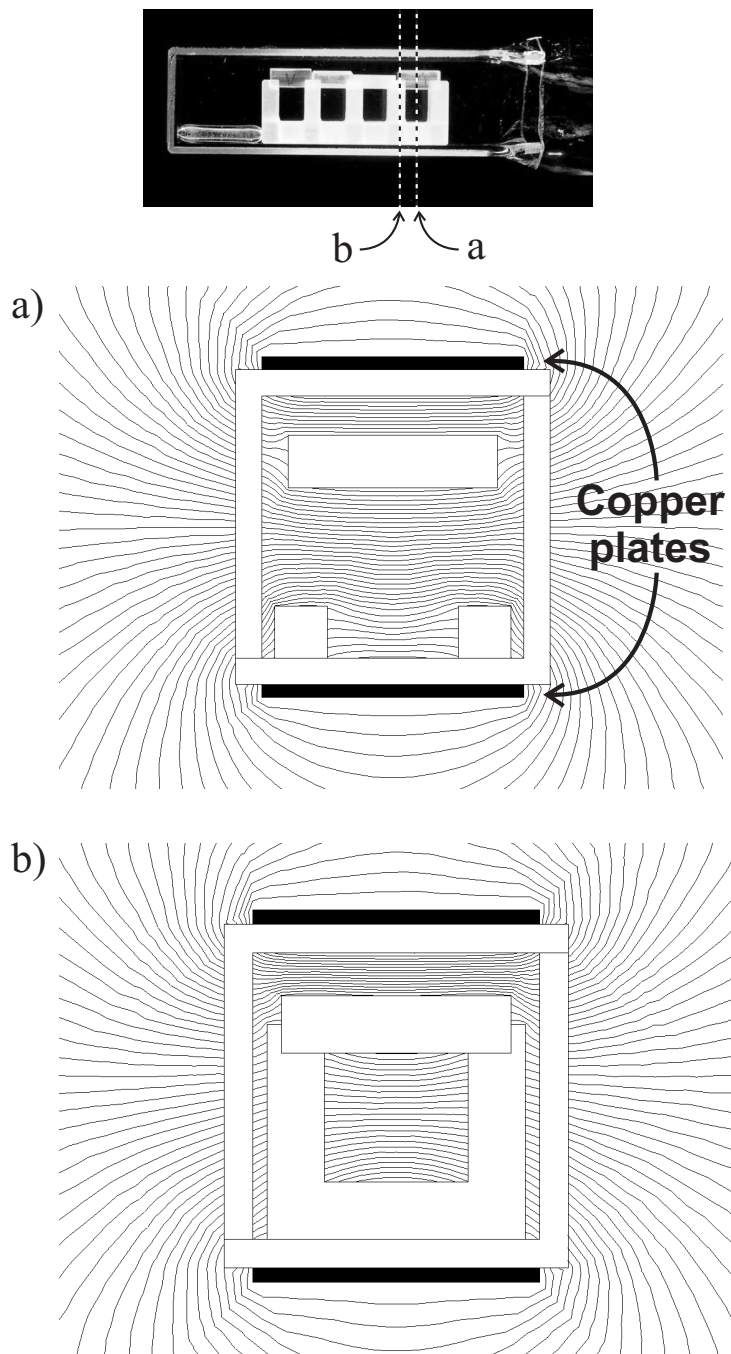


Figure 5.15: Simulation of the electric field in our science cell with the application of 100 V to the copper plates (the solid black rectangles). (a) The calculated electric potential contours (voltage contours) in a x - y slice at the axial center of a surface as depicted in the image at the top of the page. The spacing between the contours is 2 V. (b) The calculated electric potential contours in a x - y slice near the edge of the surface. The actual applied electric field for our experiments is somewhere between these two situations.

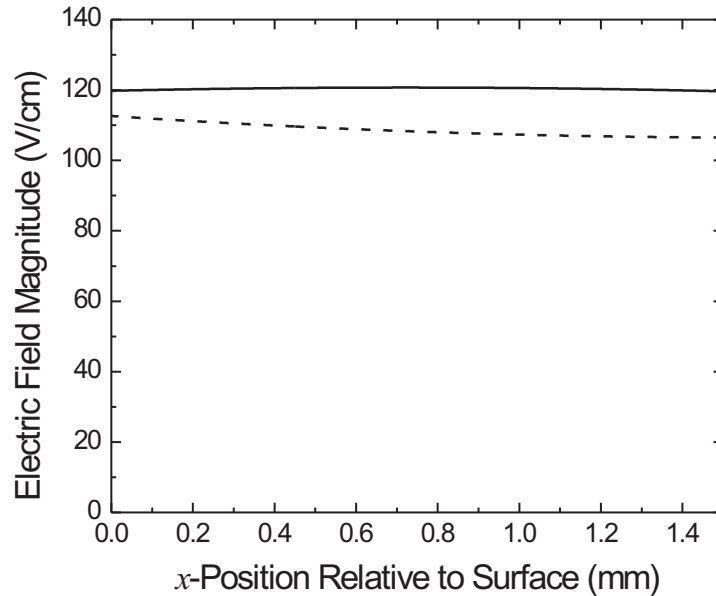


Figure 5.16: The electric field magnitude near the surface for the center (solid line, corresponding to Fig. 5.15 (a)) and edge (dashed line, corresponding to Fig. 5.15 (b)) positions. For our calculations we use a 100 V/cm as a conservative value for the applied electric field magnitude.

5.4.4 Spatially Homogeneous Magnetic Forces

Although less prevalent, evidence of magnetic surface contaminants can be seen on our insulating surface (likely remnants from surface polishing). Our trapping potential itself is magnetic so we cannot rely on techniques similar to those used for the detection of electric fields. Instead, we carefully examine the magnetic trapping potential itself. A spurious magnetic field cannot exclusively modify ω_x , rather the spurious field will manifest itself as a modification of multiple trapping frequencies, or anomalous center-of-mass displacements.

The trap frequencies in the three directions can be expressed as

$$\omega_x = \omega_y = \sqrt{\frac{\mu_B m_F g_F}{m}} \frac{\eta}{\sqrt{B_0}} \quad (5.33)$$

$$\omega_z = \sqrt{\frac{\mu_B m_F g_F}{m}} \sqrt{\beta} \quad (5.34)$$

where μ_B is the Bohr magneton, g_F is the Landé g -factor, η is the linear magnetic field gradient in the \hat{x} and \hat{y} -directions,¹⁴ B_0 is the bias field, and β is the magnetic field curvature in the \hat{z} -direction ($B_z(z) = B_0 + \beta/2 z^2$). Adding an additional spurious magnetic field B^* , and expanding to first order in B^* , the normalized frequency shift $\gamma_{x,y,z}$ induced by the spurious magnetic field can be written as

$$\gamma_x = \frac{B_z^*}{2B_0} - \frac{\partial_x B_x^*}{\eta} - \frac{B_0 \partial_x^2 B_z^*}{2\eta^2} \quad (5.35)$$

$$\gamma_y = \frac{B_z^*}{2B_0} + \frac{\partial_y B_y^*}{\eta} - \frac{B_0 \partial_y^2 B_z^*}{2\eta^2} \quad (5.36)$$

$$\gamma_z = -\frac{\partial_z^2 B_z^*}{2\beta}. \quad (5.37)$$

Invoking $\vec{\nabla} \cdot \vec{B}^* = 0$ and $\vec{\nabla} \times \vec{B}^* \simeq 0$,¹⁵ we obtain an expression for the systematic uncertainty in the normalized frequency shift caused by a spurious magnetic field, $\delta\gamma_x$, as:

$$\delta\gamma_x \simeq \sqrt{(\delta\gamma_y)^2 + \frac{B_0^2 \beta^2}{\eta^4} (\delta\gamma_z)^2 + \frac{\beta^2}{\eta^2} (\delta z_{cm})^2}, \quad (5.38)$$

where we have introduced $\delta\gamma_y$ and $\delta\gamma_z$, which are the measured systematic limits on deviations from zero of γ_y and γ_z as the condensate nears the surface, and δz_{cm} , which is the uncertainty in the movement of the center-of-mass of the condensate in the \hat{z} -direction from its equilibrium position.

This technique can be summarized as follows. If the only force on the condensate is the Casimir-Polder force, then γ_y , γ_z , and z_{cm} will not change as the condensate is

¹⁴ $\vec{\nabla} \cdot \vec{B} = 0$ forces the \hat{x} and \hat{y} magnetic field gradients to be equal at the center of the trap.

¹⁵ $\vec{\nabla} \times \vec{B} \simeq 0$ because we are considering static fields in free space.

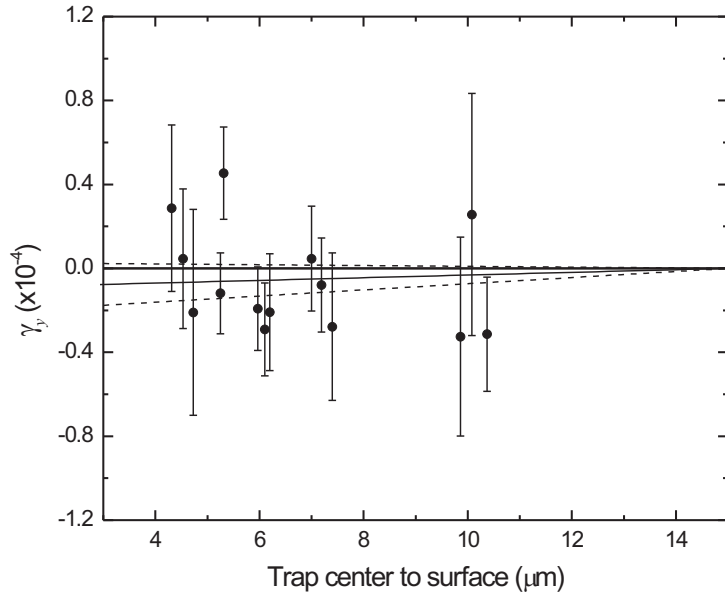


Figure 5.17: An example of γ_y measured as a function of the distance to the surface (of course in the \hat{x} -direction). This data is fit to the form $\gamma_y(x) = m(x - x_0)$ where x_0 is fixed to $15 \mu\text{m}$ (because $15 \mu\text{m}$ is the normalization distance, and thus by definition $\gamma_y(x = 15) = 0$). From this fit $m = 6.4 \pm 8.3 \times 10^{-7} \mu\text{m}^{-1}$. The fit is plotted as the solid line, and the $1\text{-}\sigma$ lines are plotted as the dotted lines. The limit with the largest absolute value is taken as the systematic limit.

moved near the surface. Therefore, if γ_y , γ_z , and z_{cm} display no statistically significant deviation, then we have verified that magnetic forces from the surface are not present at measurable levels. The uncertainty in these terms, $\delta\gamma_y$, $\delta\gamma_z$, and δz_{cm} , then allow us to obtain a systematic limit on the presence of magnetic forces.

In practice, we obtain $\delta\gamma_y$ and $\delta\gamma_z$ terms by measuring γ_y and γ_z as a function of distance to the surface; an example data showing γ_y is shown in Fig. 5.17. This data is then fit using a linear form $\gamma_{y,z}(x) = m(x - x_0)$ with x_0 fixed to $15 \mu\text{m}$. This is done because the normalization distance, by definition where $\gamma_{y,z}(x) = 0$, is $15 \mu\text{m}$. Then, the largest $1\text{-}\sigma$ is taken as the systematic limit (the larger of $|m + \sigma m|$ or $|m - \sigma m|$ is taken as the slope). For the fits shown in Fig. 5.17 the largest error is the lower $1\text{-}\sigma$ line

($\delta\gamma_y(x) = |(6.4 \times 10^{-7} + 8.3 \times 10^{-7}) \times (x - 15 \mu\text{m})|$). The absolute value of this simple linear function is then used in Eq. 5.38. A similar procedure is performed for γ_z .

To obtain δz_{cm} we measure the axial distance of the BEC at several different x -distance with respect to the surface, such as 4.2, 5, 15, 25, and 35 μm , see Fig. 5.18 (a). We fit the 15, 25, and 35 μm points to a line and subtract off the linear fit. This is done to remove any residual change in axial position as the atoms are moved to the surface [see Section 2.3.2], and the 15, 25, and 35 μm points are far away enough to not be affected by surface forces. This data is then fit (using a weighted fit) to the simple linear form:

$$z_{cm}(x) = mx + b. \quad (5.39)$$

The uncertainty in $z_{cm}(x)$, $\delta z_{cm}(x)$, is then

$$\delta z_{cm}(x) = \sqrt{(\sigma m)^2 x^2 + (\sigma b)^2}. \quad (5.40)$$

where σm and σb are the fit uncertainties in m and b respectively. Finally, the larger of $|z_{cm}(x) + \sigma \delta z_{cm}(x)|$ and $|z_{cm}(x) - \sigma \delta z_{cm}(x)|$ is taken as the full systematic uncertainty, $\delta z_{cm}(x)$, and is used in Eq. 5.38.

This technique, where we only consider uncertainties of fields, is not applicable in the case of the electrical systematics because typically a non-zero electric field is detected. Therefore, the perturbation of the measured electric field, rather than the uncertainty in the presence of an electric field, dominates the electrical systematics.

Finally, we acknowledge that in certain situations, a magnetic field could cause a change in γ_x and no change in γ_y , for instance if $B_z^*/(2B_0) = -\partial_y B_y^*/\eta$. Unlikely situations such as this cannot be categorically excluded with our current analysis technique; however by performing measurements at multiple surface locations and verifying that these measurements agree, we can reduce the possibility that this sort of unusual

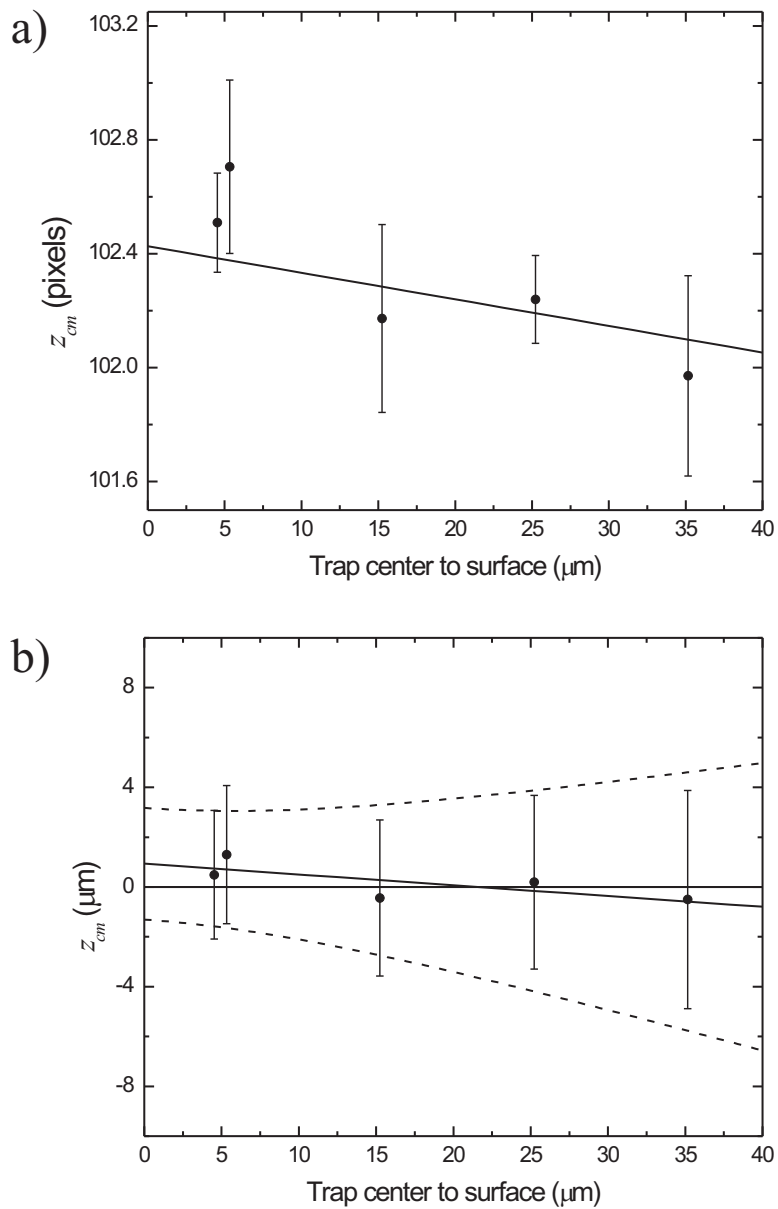


Figure 5.18: (a) The raw axial position data as a function of distance to surface. The residual slope is fit (solid line) using the 15, 25, and 35 μm points. (b) The residual slope has been subtracted off. This residual z -position data data is fit to the form (solid line) $z_{cm}(x) = mx + b$, $m = -0.04 \pm 0.13 \mu\text{m}/\mu\text{m}$ and $b = 0.9 \pm 2.2 \mu\text{m}$. The uncertainty envelope is plotted as the dashed lines.

cancellation could disturb our measurement.

5.4.5 Compensating for the Effects of Amplitude

When measuring γ_x we use an oscillation amplitude, typically $\sim 2.1 \mu\text{m}$, that is significant compared to the Thomas-Fermi radius in the \hat{x} -direction, typically $\sim 2.4 \mu\text{m}$. Because of this, we must use Eq. 5.19 when calculating the predicted γ_x for the Casimir-Polder force. For the systematic measurements that were described in the previous sections, however, the condensate is typically *not* undergoing a $2 \mu\text{m}$ oscillation in the \hat{x} -direction, so when estimating systematic limits we must compensate for this in some way.

In Fig. 5.19 (a) we plot the predicted γ_x for our typical experimental conditions (solid line). Additionally, the predicted γ_x for an oscillation amplitude of zero is plotted (dashed line). The zero amplitude curve clearly lies below the $\sim 2 \mu\text{m}$ amplitude curve.

Since we are interested in obtaining a *maximum* estimate of the systematic shifts at a given distance, what we do is associate our essentially zero amplitude (in the \hat{x} -direction) systematic measurements to γ_x data points $1 \mu\text{m}$ further from the surface [see Fig. 5.19 (b)]. For instance, we perform systematic measurements at $6 \mu\text{m}$ to obtain an estimate of the systematic shifts for the γ_x data taken at $7 \mu\text{m}$.

5.5 Casimir-Polder Results

The dielectric surfaces used for this experiment include (1) UV-grade fused silica prepared by a hydrofluoric acid etch followed by UV-ozone cleaning, (2) sapphire prepared with UV-ozone cleaning, and (3) UV-grade fused silica cleaned with acetone, ultra-pure methanol, and de-ionized water (the surfaces and surface preparation techniques are described in more detail in Section 2.2.2). Surfaces (1) and (2) displayed forces that were 3–10 times larger than the Casimir-Polder force and displayed significant spatial inhomogeneity. Previous studies of a BK7 surface had lead us to believe

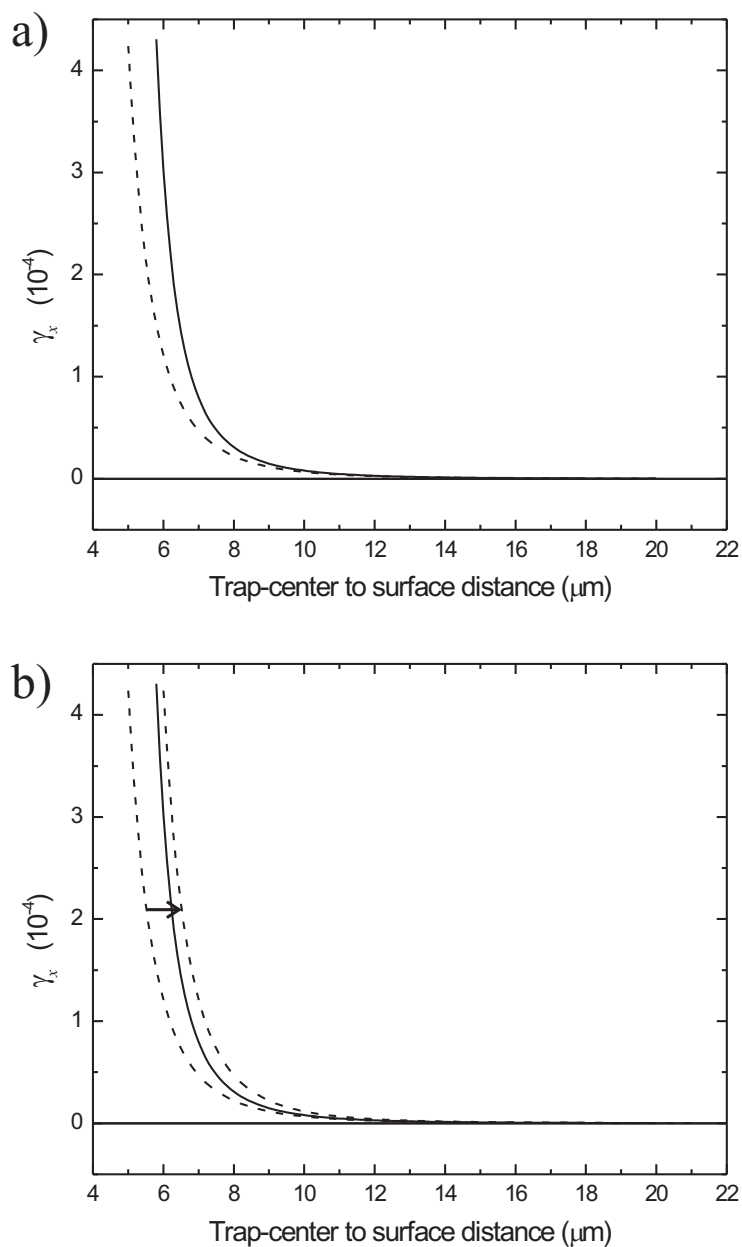


Figure 5.19: (a) The predicted γ_x from the Casimir-Polder force for an oscillation amplitude of $2 \mu\text{m}$ (solid line) and zero amplitude (dashed line). (b) If the zero amplitude curve is shifted by $1 \mu\text{m}$ it will match, or *overestimate*, the normalized frequency shift of the $2 \mu\text{m}$ oscillation amplitude curve.

Table 5.2: A summary of our statistical and systematic errors. Systematic errors are determined for each data point by evaluation of the corresponding systematic measurement data.

Error Source	Maximum (10^{-5})	Typical (10^{-5})
Statistical	8.3	4.0
Spatial Inhomogeneity	4.6	2.5
Uniform Magnetic	2.9	2.2
Uniform Electric	4.1	0.41
Normalization	0.18	0.14
Total	-	5.2

that magnetic impurities embedded during the polishing process were a problem, thus leading us to try an aggressive surface preparation such as a hydrofluoric acid etch. However, with our current surfaces, spurious forces appear to be primarily caused by spatially inhomogeneous electric surface potentials.

The fused silica surface (3) displayed the smallest level of spurious forces. Nevertheless, even with this surface we were forced to study multiple spatial locations in order to locate suitable positions for measurements. Suitable locations were primarily identified by the criteria that δ_γ is less than a certain predefined threshold value. Approximately 40% of the surface regions studied displayed spatially inhomogeneous forces. The spatially inhomogeneous forces, identified with the technique previously described, displayed peak values $\sim 100\%$ larger than the Casimir-Polder force. Spatial variations occurred on $\sim 50 \mu\text{m}$ distance scales and displayed $\sim 100\%$ percent variations in strength. It is possible that finer structure could be present, yet not detectable.

Once a suitable region was identified, we performed the experimental procedure previously outlined to measure γ_x . In addition, a significant amount of data was concurrently taken to put limits on spatially uniform electric and magnetic forces. Table 5.2 summarizes the limits from these systematic measurements. The results of our measurement of the Casimir-Polder force from surface (3) are shown in Fig. 5.20.

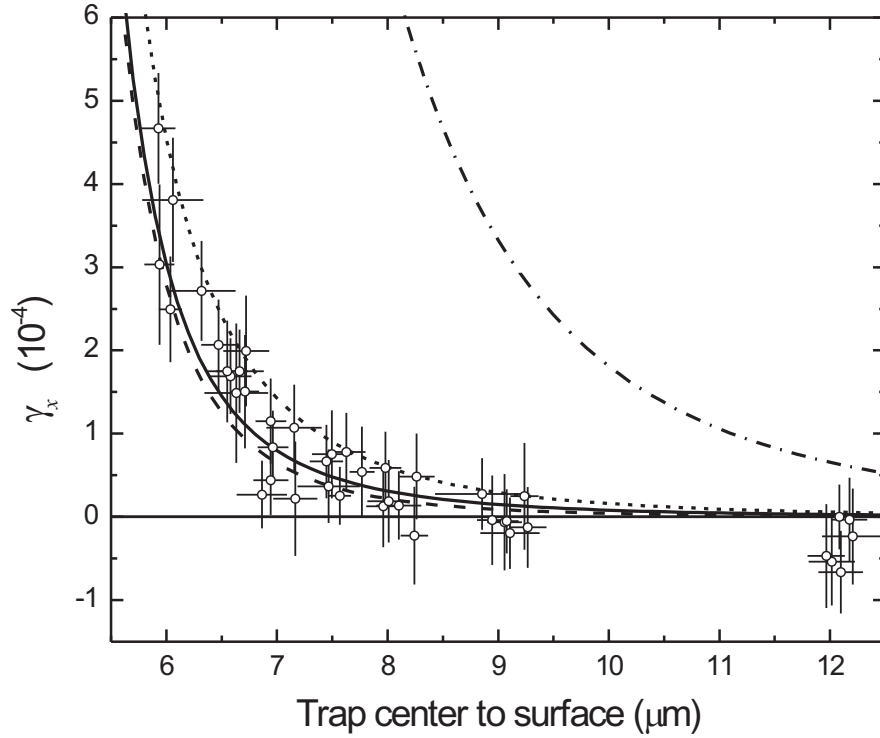


Figure 5.20: Normalized frequency shift data from the fused silica surface (DC dielectric constant = 3.83 [69]). Each data point represents a single measurement of γ_x (no data averaging was performed). This data was taken at two locations spaced $300 \mu\text{m}$ apart. Vertical error bars include the statistical and systematic errors detailed in Table I. Horizontal error bars include statistical uncertainty, surface drift, and the effects of the uncertainty in the image magnification. For this data set the mean oscillation amplitude, including the small effects of damping, is $2.06 \mu\text{m}$. The mean Thomas-Fermi radius in the \hat{x} -direction is $2.40 \mu\text{m}$ for this data. Theory lines, calculated using the theory from Antezza *et al.* [45], indicate $T = 0$ K (dash), $T = 300$ K (solid), $T = 600$ K (dot). Additionally we include the extrapolation of the van der Waals-London $1/d^3$ potential to these distances (dash-dot). For calculation of the Casimir-Polder force we utilize the static approximation of [45] that relies only on the DC dielectric constant of the substrate. The static approximation tends to slightly *overestimate* the force in the low-temperature limit. So, for the smaller trap-center to surface separations, the $T = 0$ K prediction using the full theory would be slightly further below the $T = 300$ K prediction. The size of this correction for $T = 300$ K is not enough to shift the limit curve in Fig. 6.4.

The first thing to note is that our measurement distances are deep within the retarded, or Casimir-Polder, regime. This is highlighted by the profound disagreement between the measured force and the extrapolation of the van der Waals-London force to this distance regime, as shown in Fig. 5.20. We do, on the other hand, see good agreement with the predicted Casimir-Polder force from our fused silica surface. Unfortunately, we currently do not have the experimental resolution to discern between the $T = 0$ K Casimir-Polder force and the $T = 300$ K case. Additionally, simply taking more data will not average down the errors bar in Fig. 5.20 because the contribution from the systematic errors is on the order of the statistical errors [see Table 5.5]. So, using our mechanical force measurement technique, it appears unlikely that the thermal correction to the Casimir-Polder force can be measured at room-temperature.

Repeating the measurement at an elevated temperature, however, appears promising [see Fig. 5.20 for the prediction for $T = 600$ K]. At this temperature, the predicted γ_x is larger than nearly all of our data; thus a measurement repeated at this temperature should yield a significantly larger signal. Additionally, observation of a direct correlation between a change in temperature and a corresponding increase the Casimir-Polder force would clearly demonstrate the thermal correction to the Casimir-Polder force.

Future experiments performed in non-equilibrium thermal conditions, such as holding the surface at 600 K with the surroundings at 300 K, are predicted to observe significant deviations from the equilibrium thermal Casimir-Polder case [70]. Study of the Casimir-Polder force in such non-equilibrium situations, where perhaps the delicate cancellations described in Section 5.1 are disturbed, will hopefully permit a better understanding of this often non-intuitive force.